



Earth-abundant $\text{Ni}_2\text{P}/\text{g-C}_3\text{N}_4$ lamellar nanohydrids for enhanced photocatalytic hydrogen evolution and bacterial inactivation under visible light irradiation

Wanjun Wang^a, Taicheng An^{a,*}, Guiying Li^a, Dehua Xia^b, Huijun Zhao^{c,d}, Jimmy C. Yu^e, Po Keung Wong^{b,*}

^a Guangzhou Key Laboratory of Environmental Catalysis and Pollution Control, School of Environmental Science and Engineering, Institute of Environmental Health and Pollution Control, Guangdong University of Technology, Guangzhou 510006, China

^b School of Life Sciences, The Chinese University of Hong Kong, Shatin, NT, Hong Kong SAR, China

^c Centre for Clean Environment and Energy, and Griffith School of Environment, Gold Coast Campus, Griffith University, Queensland 4222, Australia

^d Laboratory of Nanomaterials and Nanostructures, Institute of Solid State Physics, Chinese Academy of Sciences, Hefei, Anhui, China

^e Department of Chemistry, The Chinese University of Hong Kong, Shatin, N.T., Hong Kong SAR, China

ARTICLE INFO

Article history:

Received 24 April 2017

Received in revised form 6 June 2017

Accepted 10 June 2017

Available online 12 June 2017

Keywords:

Earth-abundant catalysts

Hydrogen evolution

Bacterial inactivation

$\text{g-C}_3\text{N}_4$

Ni_2P

ABSTRACT

Photocatalysts made of earth-abundant elements are highly desired for photocatalytic H_2 evolution as well as bacterial inactivation without requirement of noble metal (i.e. Pt, Ag). In this study, nickel phosphide (Ni_2P) was used as a nonprecious co-catalyst to couple with metal-free $\text{g-C}_3\text{N}_4$ based on Z-scheme type of electron transportation model. The exfoliation of bulk $\text{g-C}_3\text{N}_4$, the *in-situ* synthesis and anchoring of Ni_2P nanoparticles onto the $\text{g-C}_3\text{N}_4$ nanosheets were achieved in one-step by a hydrothermal method without adding any surfactants or templates. The optimized $\text{Ni}_2\text{P}/\text{g-C}_3\text{N}_4$ lamellar nanohydrids exhibited remarkably enhanced visible-light-driven photocatalytic activity for H_2 evolution and bacterial inactivation without noble metal loading, and the obtained activity is approximately 22 and 10 times higher than that of pure $\text{g-C}_3\text{N}_4$, respectively. The Ni_2P was proposed to effectively trap the photo-generated e^- via a Z-scheme type of route, thus significantly promoting the e^- - h^+ separation and subsequent reduction of protons to generate H_2 . The bacterial inactivation was found to undergo a direct h^+ oxidation process, and therefore the trapping of e^- by Ni_2P also facilitated h^+ accumulation, leading to enhanced bacterial inactivation efficiency. This study demonstrates a proof-of-concept for constructing all-earth-abundant photocatalysts without any noble metal elements for both energy production and environmental application.

© 2017 Elsevier B.V. All rights reserved.

1. Introduction

Energy crisis and environmental pollution are two of the major problems facing the human society. Among the numerous energy carriers, H_2 is considered to be one of the most ideal alternative candidates for the replacement of fossil fuels [1]. Since water is abundant on the Earth and it contains 11.1% hydrogen in weight, the most promising and simplest way for H_2 production is to liberate hydrogen from water. Therefore, photocatalytic H_2 production from water has attracted much attention as a potential method to convert and store inexhaustible solar energy as chemical

energy, thus solving the energy crisis problems [2,3]. Meanwhile, the elimination of pathogenic microorganisms, such as bacteria, viruses and fungi in water environments, has been one of the major tasks for wastewater treatment, as waterborne diseases have been estimated to cause 80% of illnesses in the developing country [4]. However, current water disinfection methods, such as chlorination, ozonation, and UV disinfection, have inevitable disadvantages, including secondary pollution, recolonization, safety concerns, and especially energy-consuming problems, which is unfavorable for long-term sustainable development [5,6]. Therefore, photocatalysis has also been regarded as an alternative disinfection method due to its direct utilization of solar energy to drive the microorganism inactivation process, thus accomplishing a “green”, mild and low-cost water disinfection process.

Since the pioneer report of photocatalytic H_2 production and bacterial inactivation in 1972 [7] and 1985 [8], respectively, much

* Corresponding authors.

E-mail addresses: antc99@163.com, antc99@gdut.edu.cn (T. An), pkwong@cuhk.edu.hk (P.K. Wong).

efforts have been devoted to the rational design and synthesis of inorganic semiconductors with high quantum efficiency. Among these catalytic materials, TiO_2 is the most widely investigated photocatalyst. However, the application of TiO_2 is limited by the large band gap energy of 3.2 eV, only excited with UV-light which accounts for less than 5% of the solar spectrum. Meanwhile, non- TiO_2 based semiconductors as visible-light-driven (VLD) photocatalysts has also been actively investigated, such as metal oxides [9,10], sulfides [11,12] and oxynitrides [13]. In most work reported so far, co-catalysts loaded on the surface of semiconductor are needed to enhance the photocatalytic activity. For example, Pt is indispensable for H_2 evolution to promote the separation of photoexcited charge carriers and reduce the over-potential. On the other hand, Ag element was found to play an important role in bacterial inactivation due to its excellent electron trapping ability and localized surface plasmon resonance (LSPR) effects [14]. However, the scarcity and high cost of these noble metals significantly hamper their practical and large-scale applications. Therefore, the development of novel active catalysts that are made of inexpensive earth-abundant materials is highly desirable both from environmental friendly and economic point of view.

A typical case of such earth-abundant photocatalysts is the emerged graphitic carbon nitride ($\text{g-C}_3\text{N}_4$) polymer which can be synthesized simply by thermal calcinations [15]. It has been demonstrated to be able to catalyze a variety of photoredox reactions, such as water splitting [16], CO_2 reduction [17], organics degradation [18], and bacterial inactivation [19], under visible light (VL) irradiation. However, the pristine $\text{g-C}_3\text{N}_4$ suffers from a high recombination rate of photoexcited charge carriers (i.e. e^- and h^+) as well as low photocatalytic activity [20]. A series of strategies were therefore developed to modify this metal-free catalyst, for instance by nanostructure engineering [21], metallic/nonmetallic heteroatom doping [22], crystal structure engineering [23], and heterostructure construction [24]. Le et al. has employed a hard-templating method to fabricate Cu-doped mesoporous $\text{g-C}_3\text{N}_4$, which showed 2 times higher photocatalytic degradation activity than that of pure $\text{g-C}_3\text{N}_4$ [25]. In addition, $\text{ZnO/g-C}_3\text{N}_4$ mesoporous nanocomposite has also been synthesized by similar method and found to exhibit much enhanced photocatalytic activity than that of pure $\text{mpg-C}_3\text{N}_4$ and ZnO under VL irradiation [26]. Although concrete progress has been made to enhance the photocatalytic activity of $\text{g-C}_3\text{N}_4$, most of these efforts still need noble metals (i.e. Pt) as co-catalysts especially for H_2 production. Therefore, it is very attractive to develop $\text{g-C}_3\text{N}_4$ based photocatalysts without noble metal(s), thus a genuine earth-abundant photocatalytic systems can be achieved for both H_2 production and bacterial inactivation.

Nickel phosphides comprised of inexpensive and earth-abundant elements have garnered a lot of recent interest due to their unique optoelectronic properties and potential applications [27], such as hydrodesulfurization [28], hydrodenitrification [29] and electrochemical hydrogen evolution reactions, where they benefit from low over-potentials and the largest cathodic densities among non-noble metal catalysts [30–32]. Very recently, the use of Ni_2P nanocrystals as co-catalysts was frequently extended to H_2 evolution by semiconductor photocatalysts, such as CdS [33,34], TiO_2 [35] and $\text{g-C}_3\text{N}_4$ [36], representing a rising star for the replacement of Pt as the next generation earth-abundant co-catalysts. However, these composite photocatalysts were synthesized with complicated multistep methods, or using toxic white phosphorus as the precursors, which significantly constraints their practical application. In addition, no previous study has evaluated the performances of metal phosphide as a co-catalyst for bacterial inactivation.

Herein, the first study of using metal phosphide as a non-precious co-catalyst with $\text{g-C}_3\text{N}_4$ was demonstrated for both H_2 evolution and bacterial inactivation. The $\text{Ni}_2\text{P/g-C}_3\text{N}_4$ lamellar

nanohybrids photocatalyst was synthesized for the first time by one-pot hydrothermal method with *in-situ* anchoring of Ni_2P nanocrystals onto the exfoliated $\text{g-C}_3\text{N}_4$ nanosheets, using red phosphorus as a “green”, cheap and easy-to-handle precursor. The as-prepared $\text{Ni}_2\text{P/g-C}_3\text{N}_4$ photocatalyst exhibited high photocatalytic activity in H_2 evolution and bacterial inactivation without noble metal loading under visible light irradiation. The loading amount of Ni_2P was optimized and the photocatalytic mechanisms were also investigated in detail. This work creates an avenue not only for the development of earth-abundant photocatalysts, but also for the use of metal phosphide as nonprecious co-catalysts for cost-effective H_2 production as well as water disinfection.

2. Experimental

2.1. Sample preparation

All chemicals were purchased in analytical grade and used without further purification. Bulk $\text{g-C}_3\text{N}_4$ was synthesized following the previous reference [37]. In a typical procedure, 10 g melamine was heated at 550 °C for 4 h in static air with a heating rate of 2.3 °C min⁻¹. After cooling, the resultant yellow agglomerates were milled into powder in an agate mortar for further use.

The $\text{Ni}_2\text{P/g-C}_3\text{N}_4$ was synthesized by a one-pot hydrothermal method using red phosphorus (red P), NiCl_2 and $\text{g-C}_3\text{N}_4$ as the starting materials. Typically, 0.3 g bulk $\text{g-C}_3\text{N}_4$ powder, a calculated $\text{NiCl}_2 \cdot 6\text{H}_2\text{O}$ and red P (weight ratio = 0.95:0.7) were mixed into 20 mL deionized water. The weight ratio of $\text{NiCl}_2 \cdot 6\text{H}_2\text{O}$ to red P is determined according to the previous literature [38]. The mixture was stirred for 20 min at room temperature (ca. 25 °C) and then transferred to a 25 mL Teflon stainless steel autoclave, then sealed and maintained at 140 °C for 12 h in an air dry oven. When the autoclave was cooled to room temperature, the resulting product was collected and washed with distilled water and absolute ethanol for several times. The obtained samples were dried in vacuum at 60 °C for 12 h. The as-fabricated samples are denoted as x wt% $\text{Ni}_2\text{P/g-C}_3\text{N}_4$, where “x” stands for the weight content of Ni_2P . As a reference, pure Ni_2P was also prepared as control using the same method [38].

2.2. Catalysts characterization

X-ray diffraction (XRD) patterns of the samples were recorded with a Rigaku Smart Lab X-ray diffractometer using $\text{Cu K}\alpha 1$ irradiation ($\lambda = 1.5406 \text{ \AA}$). The accelerating voltage and applied current were 40 kV and 40 mA, respectively. UV-vis diffuse reflectance spectrum (UV-vis DRS) was obtained for the dry-pressed disk sample using a Varian Cary 500 UV-vis spectrophotometer equipped with a labsphere diffuse reflectance accessory. BaSO_4 was used as a reflectance standard in the UV-vis DRS experiment. The morphology of the prepared materials was characterized by scanning electron microscopy (FESEM, FEI, Quanta 400 FEG) and transmission electron microscopy (TEM, FEI Tecnai G2 Spirit). The structure of composites was characterized by a Fourier transform infrared spectrometer (FT-IR, Nicolet 670) at a resolution of 4 cm⁻¹. The surface electronic states were analyzed by X-ray photoelectron spectroscopy (XPS, PerkinElmer PHI 5000). All the binding energy values were calibrated by using C1s = 284.6 eV as a reference. Photoluminescence spectra (PL) of the samples were obtained at room temperature excited by incident light of 375 nm [39] using a Hitachi F-4500 fluorescence spectrophotometer.

Photocurrent measurements were carried out on an electrochemical workstation (CHI 660D, Shanghai Chen Hua Instrument Company, China) with a conventional three electrode cell, using a Pt plate and a saturated Ag/AgCl electrode as counter electrode

and reference electrode, respectively. The working electrode was prepared on indium-tin oxide (ITO) glasses, which was cleaned by sonication in chloroform, acetone and ethanol for 30 min, respectively. The glass was then rinsed with water and kept in isopropanol for 24 h. Five-milligrams of samples and 10 μ L of Nafion solution (5 wt%) were dispersed in a 1 mL water/isopropanol mixed solvent (3:1 v/v) by sonication to form a homogeneous catalyst colloid. Then, 100 μ L of the catalyst colloid was deposited onto the ITO glass with areas of approximately 1 cm^2 . The working electrodes were immersed in a 0.1 M Na_2SO_4 aqueous solution without additive for 30 s before the measurement was carried out.

2.3. Photocatalytic H_2 evolution

The photocatalytic H_2 evolution experiments were carried out in a Pyrex reaction cell connected to a closed gas circulation and evacuation system. 40 mg of photocatalyst was dispersed in 50 mL of aqueous solution containing 10 vol% triethanolamine (TEOA) as a sacrificial agent. The suspension was purged with argon gas to remove dissolved air before irradiation. The solution was irradiated by a 300 W Xenon lamp (Beijing Perfect Light Co. Ltd., Beijing) equipped with a 420 nm cut-off filter. The amount of H_2 generated from photocatalytic water splitting was measured by Techcomp GC7900 gas chromatography with TCD detector and a capillary column (molecular sieve 5 \AA). High purity nitrogen gas was used as a carrier gas. Wavelength dependence of H_2 evolution rate was measured by using an appropriate band pass filter (420, 450 and 550, respectively). The intensity of the monochromatic light was averaged at 5 representative points by a light meter (LI-COR, USA) and the active area of the reactor was approximately 38.5 cm^2 . The apparent quantum efficiency (AQE) was measured and calculated according to the following Eq. (1):

$$\text{AQE} [\%] = \frac{\text{number of reacted electrons}}{\text{number of incident photons}} \times 100$$

$$= \frac{\text{number of evolved H}_2 \text{ molecules} \times 2}{\text{number of incident photons}} \times 100 \quad (1)$$

2.4. Photocatalytic bacterial inactivation

Escherichia coli K-12 was chosen as the model bacteria to evaluate the photocatalytic inactivation efficiency of the prepared photocatalysts [40]. Bacterial cells were firstly cultured in Nutrient Broth growth medium at 37 °C for 16 h with shaking, and then harvested by centrifugation at 4000 rpm for 15 min. The bacterial pellets were then washed with sterilized saline (0.9% NaCl) solution three times in a centrifuge tube and re-suspended in a sterilized saline solution to obtain suitable concentration of *E. coli*. Then, 50 mg of the as-prepared photocatalyst was added into 50 mL solution containing 10^7 cfu mL^{-1} bacterial suspensions. The solution was irradiated by a 300 W Xenon lamp equipped with a 420 nm cut-off filter. Then, at different time intervals, aliquot samples were collected and uniformly spread on Nutrient Agar plates after serial dilutions using the sterilized saline solution. The plates were incubated at 37 °C for 24 h to determine the viable cell count. All the inactivation experiments were conducted in triplicate.

3. Results and discussion

3.1. Synthesis and characterization of prepared catalyst

Fig. 1 shows the XRD patterns of as-prepared Ni_2P , $\text{g-C}_3\text{N}_4$ and $\text{Ni}_2\text{P}/\text{g-C}_3\text{N}_4$ hybrids with different Ni_2P loading amounts. The Ni_2P sample exhibits obvious diffraction peaks located at 40.8°, 44.6°, 47.3° and 54.2°, which matches well with the standard card of Ni_2P

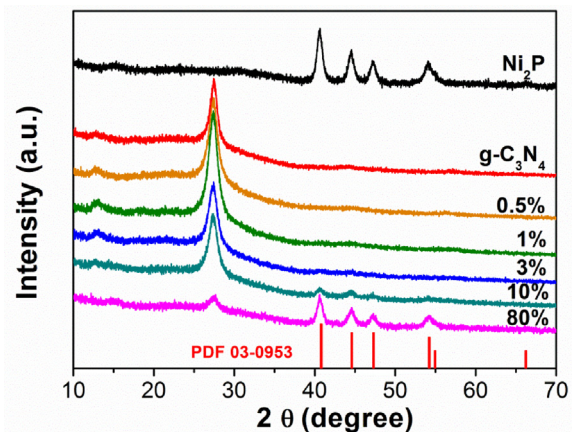


Fig. 1. X-Ray diffraction (XRD) patterns of $\text{g-C}_3\text{N}_4$, Ni_2P and $\text{Ni}_2\text{P}/\text{g-C}_3\text{N}_4$ lamellar nanohybrids with different Ni_2P loading amount.

(PDF 03-0953), confirming pure Ni_2P crystals can be successfully synthesized at the present hydrothermal condition. Meanwhile, two distinct XRD peaks at 13.0° and 27.4° are observed for pure $\text{g-C}_3\text{N}_4$ synthesized using melamine as the precursor, which are assigned to the (100) and (002) plane of the typical graphitic layer structures [41]. The peak at 13.0° is related to the in-plane repeating units of the heptazine heteroatom cycles, while the later one is assigned to the graphitic layer stacking, similar in graphite. However, the $\text{Ni}_2\text{P}/\text{g-C}_3\text{N}_4$ samples exhibit similar XRD pattern with pure $\text{g-C}_3\text{N}_4$, and no noticeable change can be found with the Ni_2P loading concentration from 0.5 to 3%, which is due to weak X-ray diffraction intensity of low concentration and highly dispersed Ni_2P nanoparticles. Similar observation was also found in Pt-loaded $\text{g-C}_3\text{N}_4$ photocatalysts [42,43]. When further increasing the loading concentration to 10 and 80%, the diffraction peaks corresponding to Ni_2P can be gradually observed, indicating the successful introduction of Ni_2P to $\text{g-C}_3\text{N}_4$ by the facile one-pot hydrothermal synthesis. The intensity of diffraction peak located at 27.4° decreases with the increase of Ni_2P amount. This is due to the increase of Ni_2P diffraction intensity and the decrease of $\text{g-C}_3\text{N}_4$ crystallinity during the hydrothermal exfoliation process.

To investigate the light harvesting property of $\text{g-C}_3\text{N}_4$, Ni_2P , as well as $\text{Ni}_2\text{P}/\text{g-C}_3\text{N}_4$ with different mass ratios, UV-vis analysis was performed and the spectra were displayed in Fig. 2. Pure $\text{g-C}_3\text{N}_4$ show typical semiconductor absorption, originating from charge transfer response of $\text{g-C}_3\text{N}_4$ from the VB populated by N 2p orbitals to the CB formed by C 2p orbitals. It shows a light absorption edge of approximately 470 nm, corresponding to the band gap energy of 2.64 eV. The tailed light absorption is attributed to the surface defects, leading to inter-band absorption. It is known that Ni_2P has a band gap of approximately 1.0 eV, corresponding to wavelength up to 1240 nm [44]. With the increase of Ni_2P addition, the color of $\text{g-C}_3\text{N}_4$ is changed from yellow to dark (Fig. 2 upper side), indicating the successful incorporation of Ni_2P . However, the absorption edge of $\text{g-C}_3\text{N}_4$ is not shifted with the increase of Ni_2P loading amount, but only the absorption intensity is enhanced in the VL region longer than 500 nm. Little change in the light absorption was observed when the Ni_2P loading amount is below 3%, indicating that Ni_2P was tightly deposited onto the surface of $\text{g-C}_3\text{N}_4$ instead of being doped into the $\text{g-C}_3\text{N}_4$ lattice.

The molecular structure information of the samples was illustrated by FT-IR spectra, as depicted in Fig. 3(A). With respect to $\text{g-C}_3\text{N}_4$, the prominent bands in the region of 1200–1650 cm^{-1} can be related to the typical stretching modes of CN heterocycles, wherein the peaks at 1241, 1318, and 1425 cm^{-1} are assigned to the aromatic C–N stretching [45,46]. The sharp band

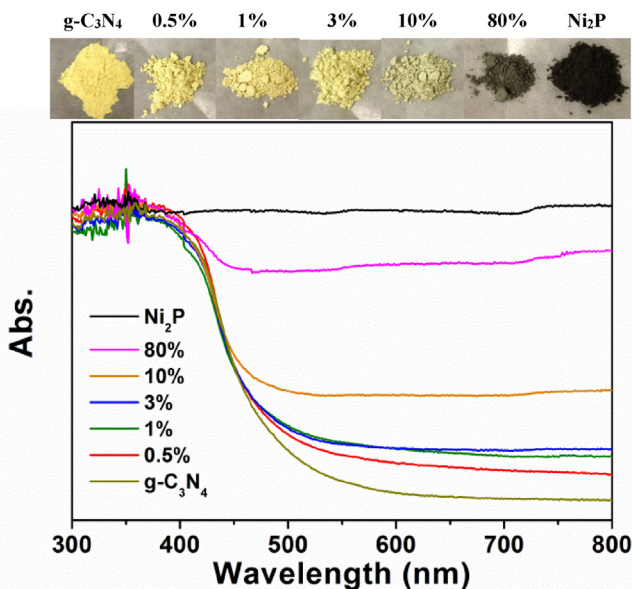


Fig. 2. UV-vis diffuse reflectance spectra (UV-vis DRS) of $\text{g-C}_3\text{N}_4$, Ni_2P and $\text{Ni}_2\text{P}/\text{g-C}_3\text{N}_4$ lamellar nanohybrids with different Ni_2P loading amount.

at 809 cm^{-1} is attributed to the out-of-plane bending vibration of characteristics of triazine rings [47]. The broad peaks at around $2600\text{--}3400\text{ cm}^{-1}$ originate from stretching vibration modes for the $-\text{NH}$ and hydroxyl group of the adsorbed H_2O . The pure Ni_2P shows a broad signal at 1080 cm^{-1} , which can be assigned to the Ni bound P=O stretching band, a natural consequence of surface oxidation in the open air [48]. This observation is similar with the results reported by Carenco et al. [49] and Senevirathne et al. [50]. The FT-IR spectrum of as-prepared $\text{Ni}_2\text{P}/\text{g-C}_3\text{N}_4$ samples signifies that the typical graphitic structure of carbon nitride was well maintained after hydrothermal reactions, while the characteristic peak corresponding to Ni_2P at 1080 cm^{-1} was also observed indicating the successful loading of Ni_2P onto $\text{g-C}_3\text{N}_4$ nanosheets. The vibration band corresponding to P-related functional groups can hardly be observed, except for a weak peak located at approximately 950 cm^{-1} (Fig. 3(B)), which is assigned to P-N stretching mode [51,52]. The peak intensity is low presumably due to the overlapping of the bands with those of strong C-N vibrations. These results indicate the Ni_2P was successfully loaded onto $\text{g-C}_3\text{N}_4$ via

P-N chemical bonding, which offers intimate and direct contact between Ni_2P and $\text{g-C}_3\text{N}_4$.

XPS spectra are recorded to analyze the surface species and chemical states of C, N, Ni, and P for typical 1% $\text{Ni}_2\text{P}/\text{g-C}_3\text{N}_4$. In high resolution XPS spectrum of C 1s (Fig. 4(A)), two deconvolution peaks at 284.6 and 288.0 eV are observed, which are assigned to graphite C-C bonds and sp^2 -hybridized carbon in N-containing aromatic ring ($\text{N}-\text{C}=\text{N}$) [53], respectively. The latter is considered as the major carbon species in $\text{g-C}_3\text{N}_4$. The high resolution N 1s spectra can be also deconvoluted into two different peaks at binding energies of 398.7 and 400.1 eV (Fig. 4(B)), corresponding to the sp^2 -hybridized nitrogen involved in triazine rings ($\text{C}-\text{N}=\text{C}$) and the tertiary nitrogen $\text{N}-(\text{C})_3$ groups, respectively [54]. For the Ni 2p region, three peaks are seen at 853.2, 856.7 and 862.5 eV (Fig. 4(C)), which is ascribed to $\text{Ni}^{\delta+}$ ($0 < \delta < 2$) in Ni_2P , oxidized Ni species (Ni^{2+}) and the satellite of the $\text{Ni} 2p_{1/2}$ peak, respectively [55]. In addition, the other three peaks at 869.5, 874.1 and 879.8 eV is corresponding to $\text{Ni}^{\delta+}$ in Ni_2P , oxidized Ni species and the satellite of the $\text{Ni} 2p_{3/2}$ peak, respectively [56]. For the P 2p energy level (Fig. 4(D)), the peak at 129.7 eV is a mark of metal-P bonds in metal phosphides (i.e. Ni_2P) [57], while the peak at 132.9 eV can be attributed to the oxidized P species due to air contact [55]. Because of the low content of Ni_2P loading, the weak XPS signals are observed for Ni 2p and P 2p. These results further confirm the formation of Ni_2P in the hybrids.

The morphologies of as-prepared $\text{Ni}_2\text{P}/\text{g-C}_3\text{N}_4$ samples were studied by SEM and TEM technology. Fig. 5(A) shows a typical SEM image of 1% $\text{Ni}_2\text{P}/\text{g-C}_3\text{N}_4$, exhibiting a lamellar structure of multilayer $\text{g-C}_3\text{N}_4$ nanosheets. It is found that the Ni_2P spherical nanoparticles are evenly decorated onto the nanosheets. TEM image in Fig. 5(B) further confirms the microstructure of the $\text{Ni}_2\text{P}/\text{g-C}_3\text{N}_4$ nanosheet hybrids, which demonstrates that it is feasible to achieve the exfoliation of $\text{g-C}_3\text{N}_4$ while *in-situ* loaded with Ni_2P nanoparticles by the one-pot hydrothermal method. In contrast, the pristine $\text{g-C}_3\text{N}_4$ clearly shows an unexfoliated large particle morphology (Fig. S1). Moreover, the lattice fringes with a spacing of 0.22 nm are evident in the high-resolution TEM image (Fig. 5(D)). The d spacing can be indexed to the high intense (111) reflection of Ni_2P [58]. The corresponding EDS spectrum in Fig. 5(C) clearly shows the elements of C, N, Ni and P, further confirming the successful formation of $\text{g-C}_3\text{N}_4$ and Ni_2P . The signals of C and Cu come from the carbon-coated copper grid substrate. The TEM images of $\text{Ni}_2\text{P}/\text{g-C}_3\text{N}_4$ samples with different Ni_2P loading amount are also presented in Fig. 6. The 0.5% $\text{Ni}_2\text{P}/\text{g-C}_3\text{N}_4$ shows a

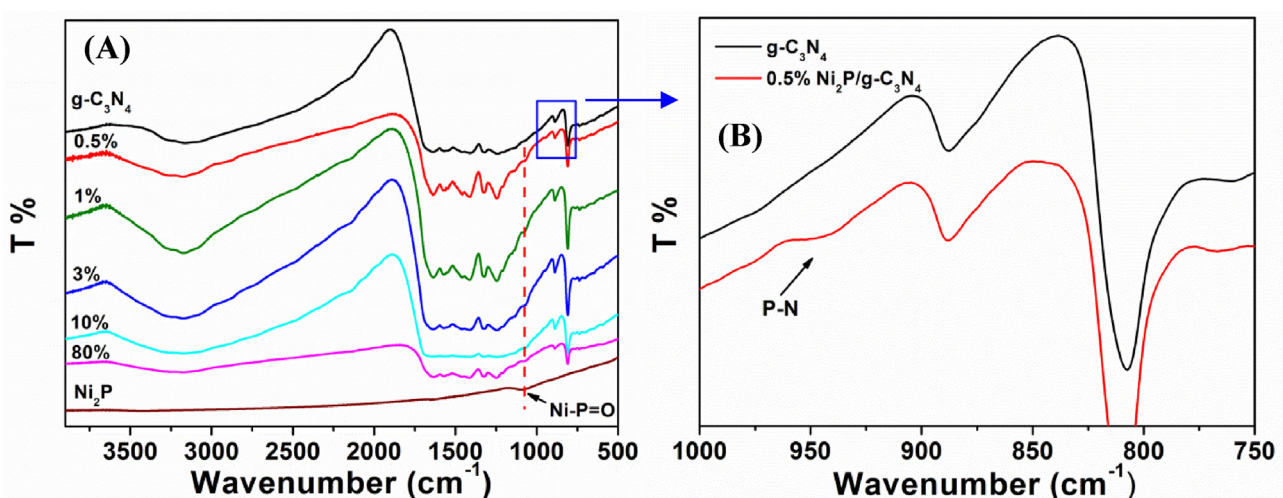


Fig. 3. (A) Fourier transform infrared (FT-IR) spectra of $\text{g-C}_3\text{N}_4$, Ni_2P and $\text{Ni}_2\text{P}/\text{g-C}_3\text{N}_4$ lamellar nanohybrids with different Ni_2P loading amount; (B) Enlarged area in plane (A).

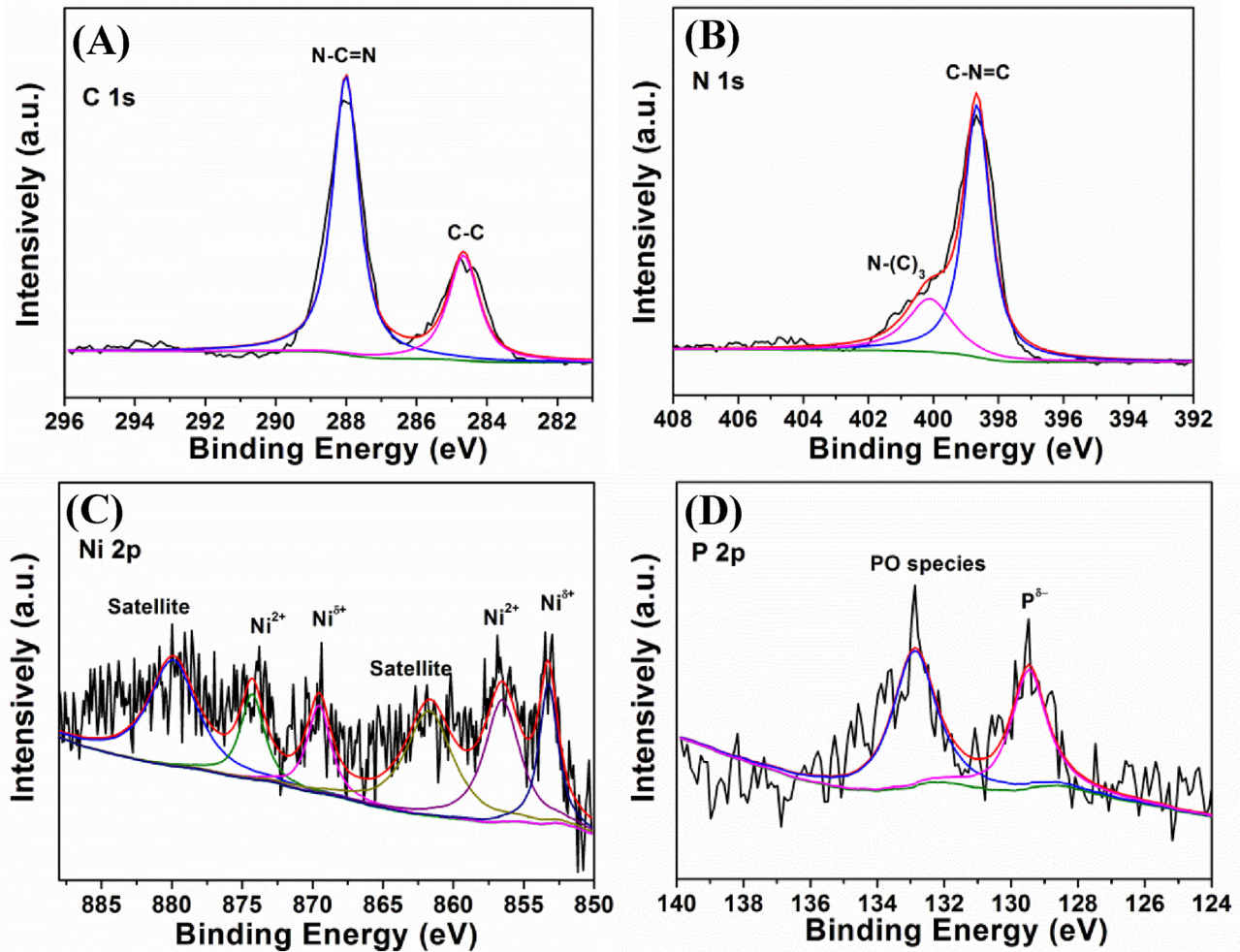


Fig. 4. High resolution X-ray photoelectron spectroscopy (XPS) spectra of 1% Ni₂P/g-C₃N₄ sample: (A) C 1s; (B) N 1s; (C) Ni 2p; (d) P 2p.

clear lamellar morphology with tiny Ni₂P nanoparticles (Fig. 6(A)), indicating small amount of Ni²⁺ is enough to help exfoliating the g-C₃N₄. With increasing Ni₂P content, the Ni₂P nanoparticles with sizes of 10–50 nm grow bigger and gradually are aggregated together (Fig. 6(B–E)). It is found that high amount of Ni²⁺ addition (>10% Ni₂P) would result in the deterioration of g-C₃N₄ exfoliation efficiency, leading to the formation of unexfoliated Ni₂P/g-C₃N₄ aggregates, which is unfavorable for photocatalytic reactions.

Based on the above results, the exfoliation of g-C₃N₄ and its induced *in-situ* anchoring of Ni₂P synthesis process is illustrated in Fig. 7. At the initial stage, the divalent nickel ions with ionic radius of approximately 0.07 nm are inserted into the layered g-C₃N₄ material. Subsequently, the inserted Ni²⁺ cations react with red P to produce Ni₂P nucleus, which then undergo slow heterogeneous nucleation, restricted growth and finally come into being crystalline Ni₂P nanoparticles anchored onto the layered g-C₃N₄, and this process in turn promotes the self-exfoliation of bulk g-C₃N₄, resulting in *in-situ* fabrication of lamellar Ni₂P/g-C₃N₄ nanohybrids. To further prove this mechanism, hydrothermal treatment of bulk g-C₃N₄ without Ni²⁺ addition was also conducted, and the results show that only particles of g-C₃N₄ can be obtained (Fig. S2), confirming the crucial role of Ni²⁺ for the exfoliation of g-C₃N₄. This Ni²⁺-induced exfoliation mechanism is expected to find applications for exfoliating other lamellar materials, especially for simultaneous anchoring with Ni species.

3.2. Photocatalytic H₂ evolution performances

The photocatalytic hydrogen production activities of the as-prepared samples were evaluated with TEOA as a sacrificial agent under visible light irradiation. Fig. 8(A) shows the H₂ evolution activity of Ni₂P/g-C₃N₄ lamellar nanohybrid photocatalysts with different loading amounts of Ni₂P. Notably, the yield of H₂ increases linearly with increasing reaction time over all the Ni₂P/g-C₃N₄ samples. The H₂ evolution efficiency is calculated and shown in Fig. 8(B). Pure g-C₃N₄ and Ni₂P nanoparticles are used for the comparison. No appreciable H₂ is observed when Ni₂P alone is used under visible light irradiation, revealing that Ni₂P is not an active photocatalyst for H₂ evolution, probably due to its small band gap (1.0 eV). The g-C₃N₄ shows little photocatalytic activity for H₂ evolution ($\sim 16.4 \mu\text{mol h}^{-1} \text{g}^{-1}$) without noble metal loading, which is in agreement with previous studies that noble metal loading is indispensable for g-C₃N₄ photocatalytic system [59]. Interestingly, with only 0.5% of Ni₂P loaded on g-C₃N₄ to produce Nanohybrid, the Ni₂P/g-C₃N₄ photocatalysts exhibits a significantly enhanced H₂ evolution rate of 169.1 $\mu\text{mol h}^{-1} \text{g}^{-1}$. With increasing loading amounts of Ni₂P, the H₂ evolution rate is increased accordingly. The highest photocatalytic H₂ evolution rate is achieved with 1% Ni₂P loading, providing an extraordinary H₂ evolution rate of 362.4 $\mu\text{mol h}^{-1} \text{g}^{-1}$, which is approximately 22 times higher than that of g-C₃N₄ alone. However, further increasing the content of Ni₂P would result in the decrease of the photocatalytic activity. It is found that the H₂ evolution rate is gradually reduced to 248.8,

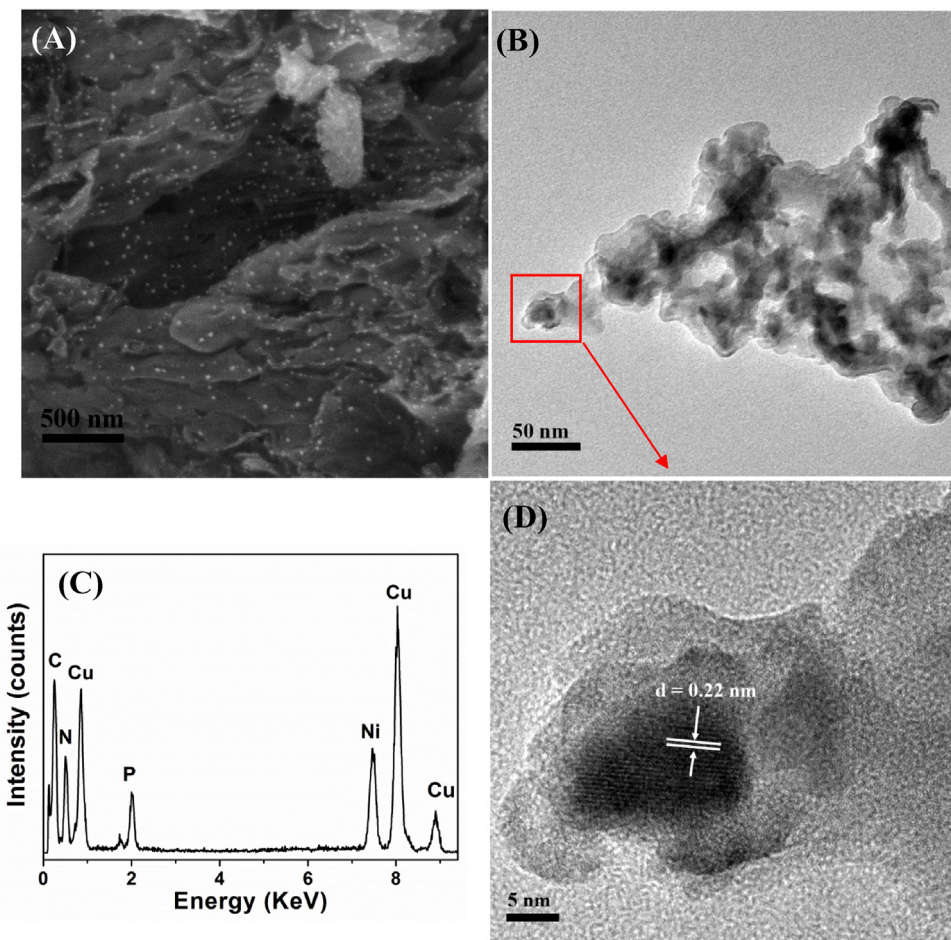


Fig. 5. (A) Typical scanning electron microscopy (SEM) image, (B) Transmission electron microscopy (TEM) image, (C) Energy-dispersive X-ray (EDX) spectrum and (D) High resolution transmission electron microscopy (HRTEM) image of 1% Ni₂P/g-C₃N₄.

175.2 and 35.2 $\mu\text{mol h}^{-1} \text{ g}^{-1}$ for the samples with 3, 10 and 80% Ni₂P loading, respectively.

As known, Pt is the most commonly used noble metal co-catalyst to enhance the H₂ evolution activity. Therefore, the photocatalytic H₂ evolution activity of 1% Pt/g-C₃N₄ was measured to compare with 1% Ni₂P/g-C₃N₄ under the same reaction conditions. The results show that the H₂ evolution amount increases linearly with time in both systems of Pt/g-C₃N₄ and Ni₂P/g-C₃N₄, while the Ni₂P/g-C₃N₄ exhibits obvious higher rate than that of Pt/g-C₃N₄ (Fig. S3), demonstrating that Ni₂P is a good noble-metal-free co-catalyst coupled with g-C₃N₄ under visible light irradiation. The apparent quantum efficiency (AQE) at 420 nm was evaluated by measuring the H₂ production rate under monochromatic light ($\lambda = 420 \text{ nm}$) irradiation. The calculated AQE is approximately 1.8% and maintains stable for 6 h of visible light irradiation (Fig. S4). It was found the value was lower in the first hour (1.57%), which may be due to an induction period at the early stages and the dissolved H₂ in the solution [60]. Moreover, the wavelength dependence of photocatalytic H₂ evolution was also investigated in the range of 420–550 nm using various band pass filters ($\lambda = 420, 450, 500$ and 550 nm). As shown in Figs. 8(C) and S5, the photocatalytic H₂ production rate under different wavelengths matches very well with its light absorption property, indicating the H₂ evolution is indeed a light-induced catalytic reactions. Notably, the longest wavelength used for H₂ evolution is extended to 550 nm, which is attributed to the efficient electron trapping ability of Ni₂P as the co-catalysts. In addition, the photo-stability was also evaluated by performing recycling experiments. As shown in Fig. 8(D), the H₂ evolution

yield remains unchanged after five runs under visible light irradiation (total for 30 h), confirming the sufficient stability of hybrid Ni₂P/g-C₃N₄ catalyst for photocatalytic H₂ evolution.

3.3. Photocatalytic bacterial inactivation performances

The photocatalytic disinfection activity was also evaluated by inactivating *E. coli* K-12 as a representative waterborne microorganism. As shown in Fig. 9(A), the g-C₃N₄ and Ni₂P nanoparticles shows similar bacterial inactivation activity, and less than 2.5-log cfu mL⁻¹ *E. coli* K-12 can be inactivated within 4 h of visible light irradiation. Interestingly, with only 0.5% Ni₂P loading, the as-prepared Ni₂P/g-C₃N₄ sample exhibits obvious enhanced photocatalytic bacterial inactivation activity (3-log cfu mL⁻¹ cell reduction within 4 h), and the inactivation efficiency is found to further increase with the increase of Ni₂P loading amount. The highest activity is observed from 10% Ni₂P/g-C₃N₄ photocatalyst, on which total 7-log cfu mL⁻¹ cell reduction is completely achieved within 4 h. The photocatalytic bacterial inactivation activity of 10% Ni₂P/g-C₃N₄ is compared with that of 10% Pt/g-C₃N₄. The results show that only approximately 3.5-log cfu mL⁻¹ cell reduction is obtained with Pt/g-C₃N₄ under the same condition (Fig. S6), indicating the Ni₂P/g-C₃N₄ also shows much higher photocatalytic bacterial inactivation activity than that of Pt/g-C₃N₄. It is obvious that the intimate heterojunctions between g-C₃N₄ and Ni₂P play the important role in determining the high photocatalytic activity. It is also noted that no bacterial cells are inactivated in light control experiments, while a very slight reduction of cell density in dark with 10% Ni₂P/g-C₃N₄

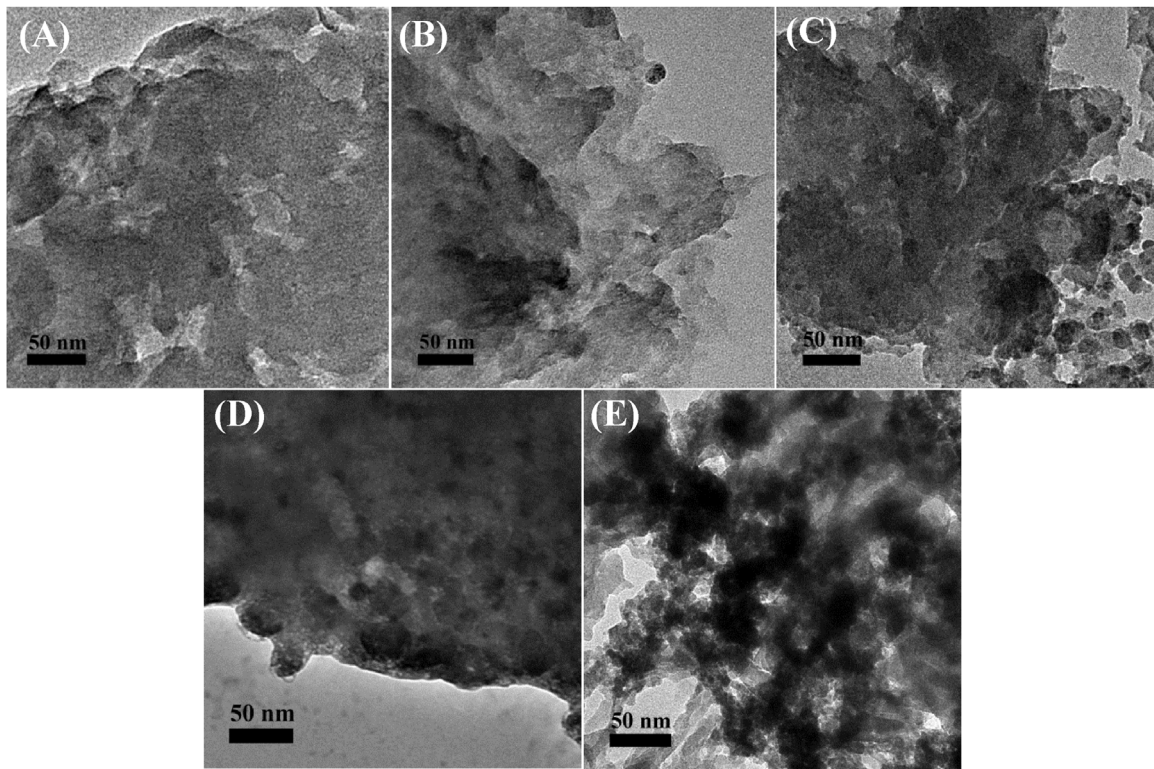


Fig. 6. Transmission electron microscopy (TEM) images of lamellar Ni₂P/g-C₃N₄ nanohybrids with different Ni₂P loading amount: (A) 0.5%; (B) 1%; (C) 3%; (D) 10%, (E) 80%.

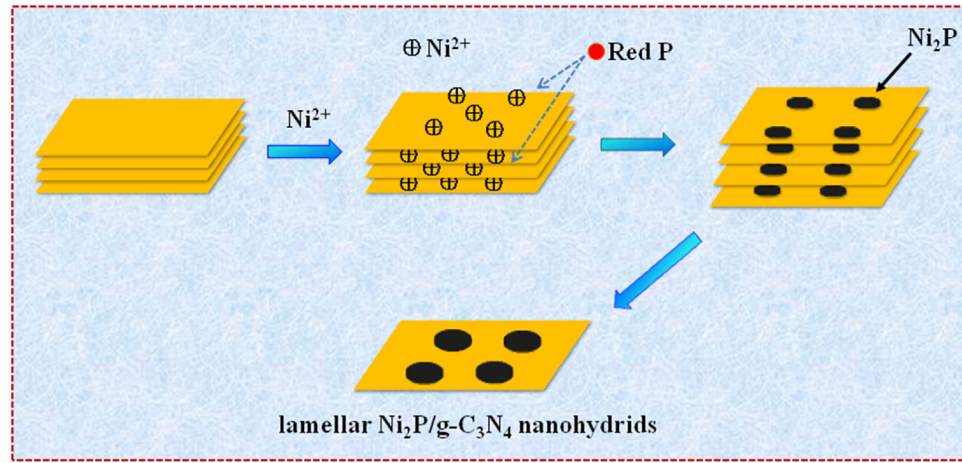


Fig. 7. Schematic illustration of the formation process of lamellar Ni₂P/g-C₃N₄ nanohybrids.

is observed, probably due to the intrinsic antibacterial property or the adsorption of Ni₂P nanoparticles.

To quantitatively understand the reaction rate, the inactivation kinetics were also modeled with a first-order decay of viability, followed by the presence of a tailing phase in which liberated intracellular components competing with the intact cell for the photocatalytic attack. These results were fitted well ($R^2 = 0.99$) using the model proposed by Geeraerd et al. [61] (Eq. (2)):

$$N_t = (N_0 - N_{\text{res}}) \times \exp(-k_{\text{max}} \times t) + N_{\text{res}} \quad (2)$$

Where N_t and N_0 was the survival number of cells at reaction time (t) and initial time, respectively; k_{max} denoted the inactivation rate and N_{res} was the residual number of the cells, and the fitted k_{max} values are shown in Fig. 9(B). The pure g-C₃N₄ and Ni₂P nanoparticles show a k_{max} value of only 0.07 and 0.13, respectively.

With the increase of Ni₂P loading amount, the k_{max} values increases from 0.53 to 0.71, and then decreases to 0.63 for 80% Ni₂P/g-C₃N₄. Therefore, the 10% Ni₂P/g-C₃N₄ exhibits significantly enhanced photocatalytic bacterial inactivation efficiency by a factor of at least 10 times higher than that of pure g-C₃N₄. It is noted that the optimal Ni₂P loading amount for H₂ evolution is 1%, while this is 10% for bacterial inactivation. The difference can be rationalized by considering the intrinsic antibacterial property of Ni₂P, which contribute to the bacterial inactivation efficiency but not for H₂ evolution. Therefore, with more Ni₂P loading beyond 1%, the bacterial inactivation efficiency can be further improved, and the optimal amount of Ni₂P increases to 10%.

To understand the bacterial inactivation mechanism during the photocatalytic process, scavenging studies was conducted by using isopropanol, Cr(VI), Fe(II)-EDTA and oxalate as •OH, e⁻, H₂O₂ and

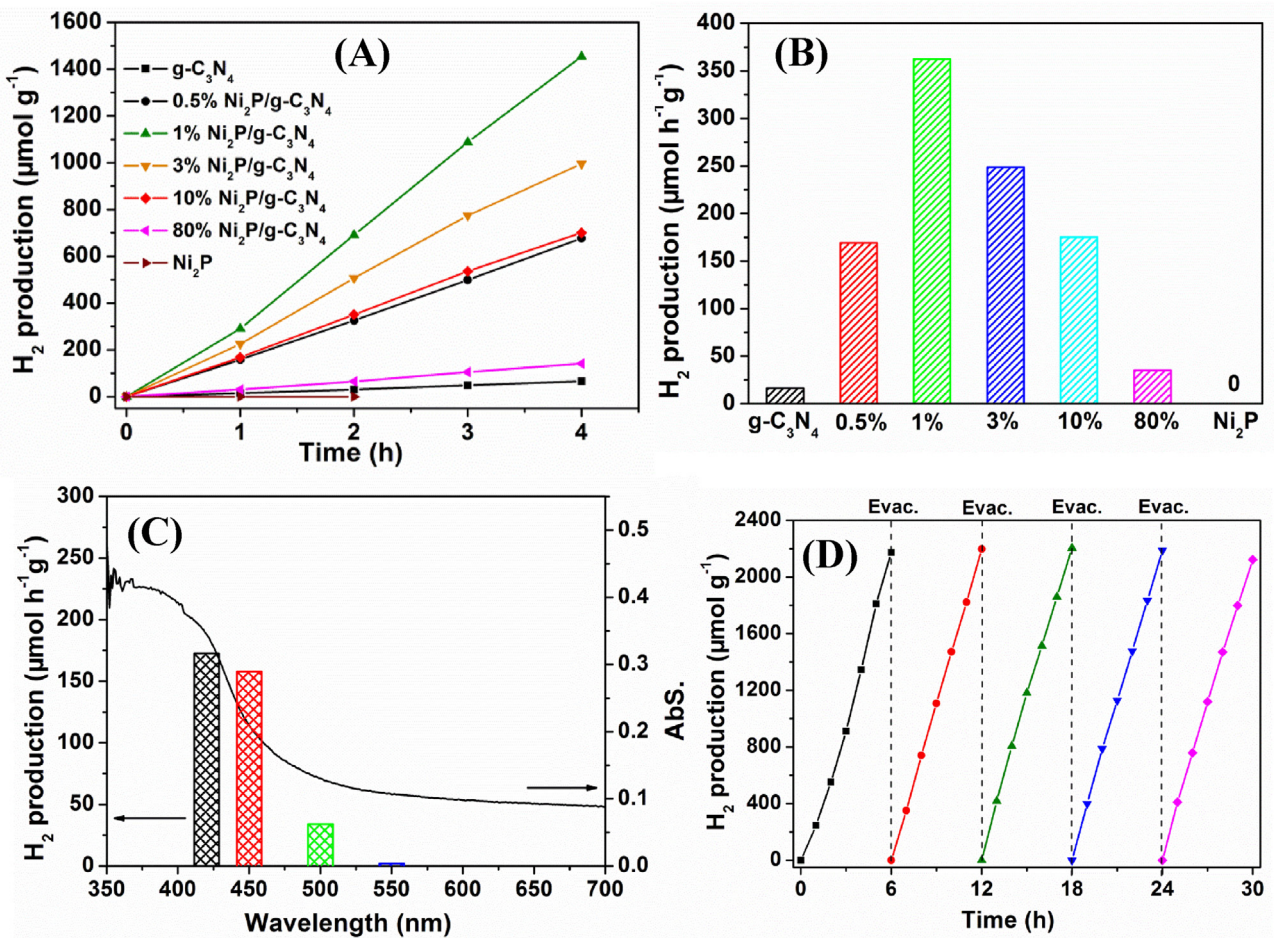


Fig. 8. (A) Photocatalytic H₂ evolution by as-prepared samples under VL irradiation; (B) Normalized H₂ evolution rate within 4 h; (C) Wavelength-dependent photocatalytic H₂ evolution over 1% Ni₂P/g-C₃N₄ under different monochromic light irradiation; (D) Cyclic H₂ evolution curve for 1% Ni₂P/g-C₃N₄ sample under VL irradiation.

h⁺ scavengers, respectively, with the method recommended by the reference [62]. No bacterial inactivation was observed with the addition of these scavengers (Fig. S7), indicating the present dosage of scavengers would not cause detectable toxicity to the bacterial cells. As shown in Fig. 9(C), the addition of isopropanol and Cr(VI) has little influence on the photocatalytic bacterial inactivation efficiency, indicating the •OH and e⁻ are not directly involved in the inactivation process. With the addition of Fe(II)-EDTA, the inactivation efficiency is decreased significantly, suggesting H₂O₂ is important for the inactivation in this system. However, the addition of oxalate almost completely inhibits the inactivation process, which indicates that the h⁺ may be the major reactive species for the bacterial inactivation, and the H₂O₂ is produced from h⁺ at the valence band of g-C₃N₄ [40,63]. To evaluate the photocatalytic stability, the bacterial inactivation treatment was also repeated five times with the same 10% Ni₂P/g-C₃N₄ sample (Fig. 9(D)). Results showed that no obvious deterioration of inactivation efficiency was observed in the first four runs, confirming the high photo-stability of Ni₂P/g-C₃N₄ although there was a slight decrease in inactivation efficiency in the fifth run, probably due to the loss of catalysts during the repeated cycling experiments.

3.4. Photocatalytic mechanisms

To understand the effects of Ni₂P loading on the photo-generated e⁻-h⁺ separation, migration and transfer during the photocatalytic process, the band structures of g-C₃N₄ and Ni₂P were studied. It is generally known that the conduction band (CB)

and valence band (VB) potentials designated as E_{CB} and E_{VB} can be estimated according to the following empirical Eqs. (3) and (4):

$$E_{CB} = E_{VB} - E_g \quad (3)$$

$$E_{VB} = X - E_e + 0.5E_g \quad (4)$$

Where the E_g, X and E_e are the band gap energy, absolute electronegativity of the semiconductor and the energy of free electrons on the hydrogen scale (approximately 4.5 eV), respectively [64,65]. Based on the result of UV-vis spectra, the g-C₃N₄ has band gap energies of 2.64 eV, while the Ni₂P has a band gap of 1.0 eV [44]. According to the calculations, the CB and VB potentials of g-C₃N₄ are approximately -1.15 and 1.49 eV, while the CB and VB potentials of Ni₂P are approximately -1.23 and -0.23 eV, respectively. As shown in Fig. 10, The CB of g-C₃N₄ is more positive than that of Ni₂P while more negative than the VB of Ni₂P, thus allowing photogenerated electrons excited from the VB of g-C₃N₄ could subsequently transfer to the VB of Ni₂P under visible light illumination, forming a Z-scheme type of electron transportation. The SEM and TEM results confirm the intimate contact of Ni₂P and g-C₃N₄ in the Ni₂P/g-C₃N₄ nanohybrid, which facilitates the efficient transfer of photogenerated carriers. The Ni₂P acts as the electron sinker and promoter which traps the photogenerated e⁻ from g-C₃N₄, and promotes the electron energy level, so that H₂O/H⁺ can be more easily to be reduced. In addition, the excellent electrochemical proton reduction property of Ni₂P as well as the weak binding property of hydrogen on Ni₂P surface also reduces the energy cost for hydrogen evolution [66]. On the other hand, since the major reactive species

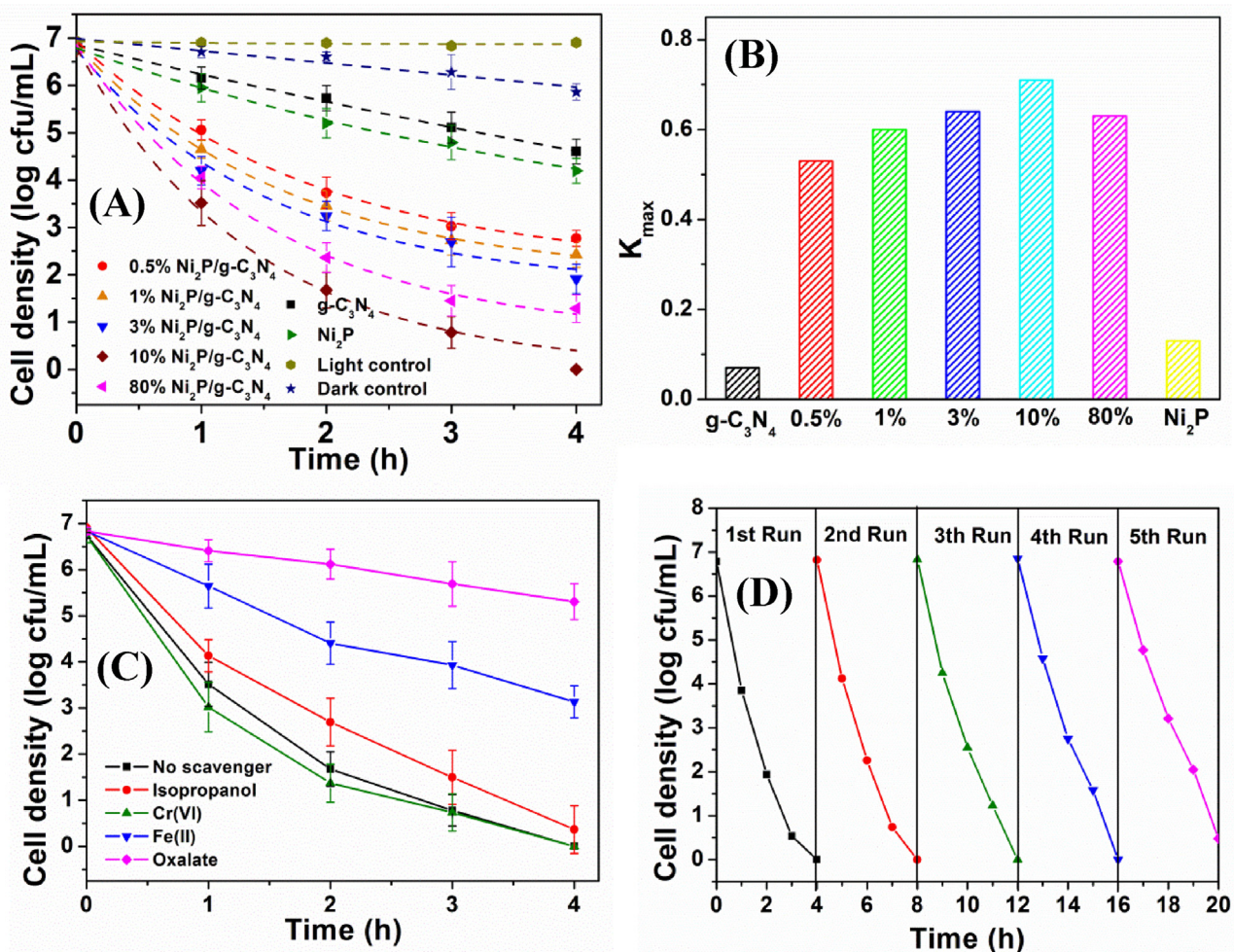


Fig. 9. (A) Photocatalytic inactivation efficiencies against *E. coli* K-12 by as-prepared samples with kinetic modeling; (B) Fitted reaction rate constant K_{\max} ; (C) Photocatalytic inactivation efficiencies against *E. coli* K-12 by as-prepared samples with different scavengers (0.05 mM Cr(VI), 0.5 mM isopropanol, 0.5 mM sodium oxalate, 0.1 mmol/L Fe(II)-EDTA); (D) Recycling experiments of photocatalytic inactivation against *E. coli* K-12 by 10% $\text{Ni}_2\text{P}/\text{g-C}_3\text{N}_4$ under VL irradiation.

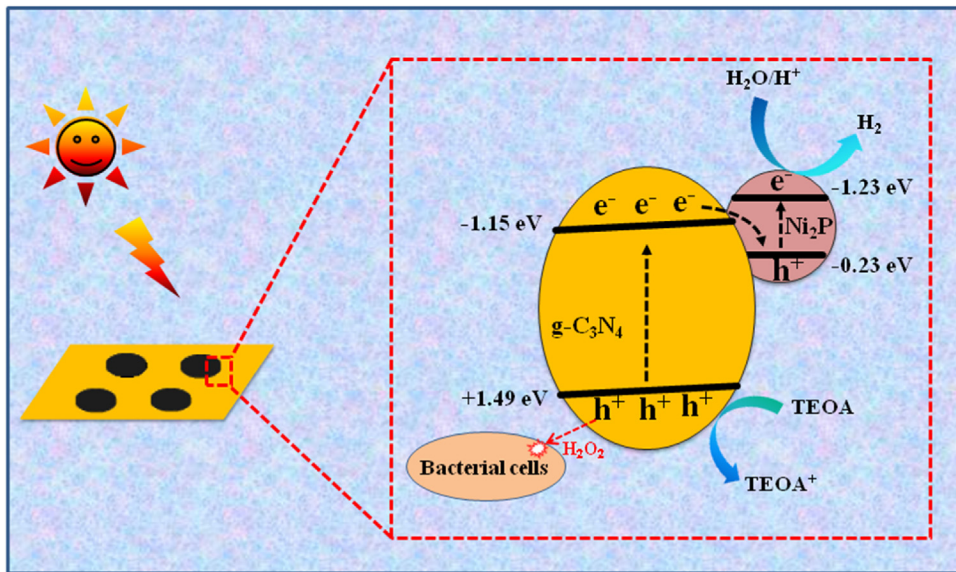


Fig. 10. Schematic illustration of the photocatalytic mechanisms of $\text{Ni}_2\text{P}/\text{g-C}_3\text{N}_4$ lamellar nanohybrids in H_2 evolution and bacteria inactivation.

for bacterial inactivation in this case is photo-generated h^+ , the excellent electron trapping property of Ni_2P favors the suppression

of $e^- - h^+$ recombination, thus more h^+ can be used for bacterial inactivation, which endows the Ni_2P to be a good co-catalysts for

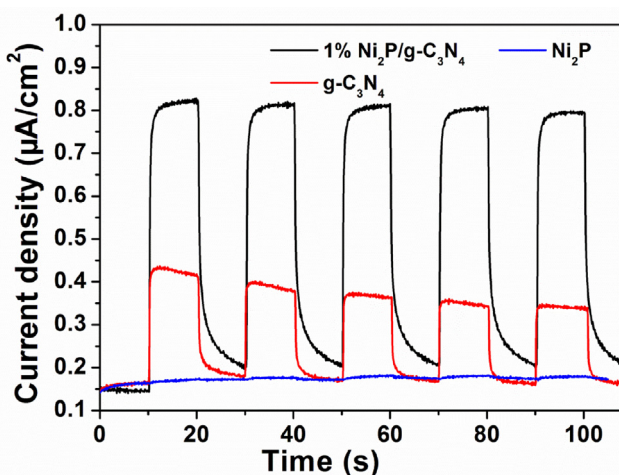


Fig. 11. Transient photocurrent responses of $\text{g-C}_3\text{N}_4$, Ni_2P and 1% $\text{Ni}_2\text{P}/\text{g-C}_3\text{N}_4$.

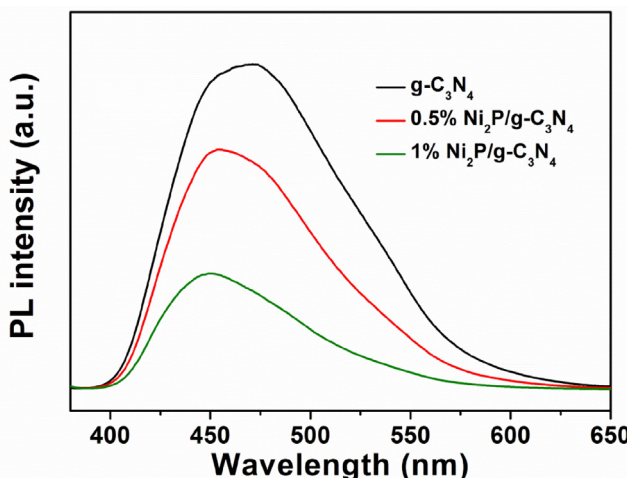


Fig. 12. Photoluminescence spectra of $\text{g-C}_3\text{N}_4$, 0.5% and 1% $\text{Ni}_2\text{P}/\text{g-C}_3\text{N}_4$ lamellar nanohybrids excited at 375 nm.

photocatalytic bacterial inactivation. The similar results was also obtained from our early two references that the h^+ from the VB of $\text{g-C}_3\text{N}_4$ really can be successfully applied in the transformation of emerging contaminants and the inactivation of bacteria [67,68].

To reveal the migration, transfer and recombination processes of photogenerated e^- - h^+ pairs in semiconductors, the photoelectrochemical experiments were conducted and the photocurrent response was also measured. As shown in Fig. 11, the photocurrent responses for the $\text{Ni}_2\text{P}/\text{g-C}_3\text{N}_4$ composite electrode is prompt, steady and reproducible during repeated on/off cycles of the visible light illumination. The $\text{g-C}_3\text{N}_4$ shows moderate photocurrent intensity, while the photocurrent is significantly increased with the loading of 1% Ni_2P , suggesting the enhanced migration efficiency of photo-induced charge carriers. Moreover, the charge separation efficiency was further examined by photoluminescence (PL) technique reported from the reference [69]. Fig. 12 presents the photoluminescence spectra of pure $\text{g-C}_3\text{N}_4$ and $\text{Ni}_2\text{P}/\text{g-C}_3\text{N}_4$ lamellar nanohydrd. The excitation wavelength of $\text{g-C}_3\text{N}_4$ is 375 nm according to the previous reference [39]. The strong and wide PL emission peak of $\text{g-C}_3\text{N}_4$ is clearly decreased after loading only 0.5% Ni_2P co-catalyst, followed by further decreasing with 1% Ni_2P loading, indicating that the recombination of electrons and holes is hindered significantly with increasing Ni_2P loading amount. These results confirm that the incorporation of Ni_2P as co-catalysts could

effectively facilitates the electron–hole separation, migration and transfer at the catalyst interfaces, thus finally enhancing the photocatalytic efficiency of both H_2 evolution and bacterial inactivation.

4. Conclusions

In summary, Ni_2P -loaded $\text{g-C}_3\text{N}_4$ lamellar nanohydrd photocatalysts were successfully synthesized by a one-step hydrothermal method based on Z-scheme type of electron transportation model. The exfoliation of $\text{g-C}_3\text{N}_4$, the formation and *in-situ* anchoring of Ni_2P nanocrystals onto $\text{g-C}_3\text{N}_4$ nanosheet were achieved simultaneously without adding any surfactants or template, which is easy to scale up for practical applications. The Ni_2P was loaded onto $\text{g-C}_3\text{N}_4$ via P-N chemical bonding, offering intimate contact between Ni_2P and $\text{g-C}_3\text{N}_4$ nanosheet. The as-prepared $\text{Ni}_2\text{P}/\text{g-C}_3\text{N}_4$ showed much enhanced photocatalytic activity in H_2 evolution without noble metal loading, with 22 times efficiencies higher than that of $\text{g-C}_3\text{N}_4$ nanosheets. In addition, it also exhibited enhanced photocatalytic bacterial inactivation activity by a factor of 10 times under visible light irradiation. Thus Ni_2P could effectively trap the photogenerated e^- via a Z-scheme type of route, and significantly promoting the e^- - h^+ separation and subsequent reduction of protons to generate H_2 . The efficient trapping of e^- would in turn promote the h^+ accumulation in the VB for bacterial inactivation, making the $\text{Ni}_2\text{P}/\text{g-C}_3\text{N}_4$ a good bacterial inactivation photocatalysts. Most importantly, this reaction system made of earth-abundant elements would serve as a typical example for constructing “green” and environmental friendly catalysts, thus solving both the energy crisis and environmental pollution problems in a cost-effective and sustainable manner.

Acknowledgements

This work was supported by the National Natural Science Foundation of China (No. 41425015, 21607028 and 41573086) and the Research Grant Council of Hong Kong SAR Government (GRF14100115) to T.C. An, W.J. Wang, G.Y. Li and P.K. Wong, respectively. H.J. Zhao and P.K. Wong were also supported by CAS/SAFEA International Partnership Program for Creative Research Teams (2015HSC-UE004) of Chinese Academy of Sciences.

Appendix A. Supplementary data

Supplementary data associated with this article can be found, in the online version, at [10.1016/j.apcatb.2017.06.027](https://doi.org/10.1016/j.apcatb.2017.06.027).

References

- [1] A.J. Esswein, D.G. Nocera, Chem. Rev. 107 (2007) 4022–4047.
- [2] D. Lu, T. Takata, N. Saito, Y. Inoue, K. Domen, Nature 440 (2006) 295–295.
- [3] R.M. Navarro, M.C. Sánchez-Sánchez, M.C. Alvarez-Galvan, F. del Valle, J.L.G. Fierro, Energy Environ. Sci. 2 (2009) 35–54.
- [4] W.J. Wang, G.Y. Li, D.H. Xia, T.C. An, H.J. Zhao, P.K. Wong, Environ. Sci.: Nano 4 (2017) 782–799.
- [5] O.K. Dalrymple, E. Stefanakos, M.A. Trotz, D.Y. Goswami, Appl. Catal. B: Environ. 98 (2010) 27–38.
- [6] E.M. Anastasi, T.D. Wohlsen, H.M. Stratton, M. Katouli, Water Res. 47 (2013) 6670–6679.
- [7] A. Fujishima, K. Honda, Nature 238 (1972) 37–38.
- [8] T. Matsunaga, R. Tomoda, T. Nakajima, H. Wake, FEMS Microbiol. Lett. 29 (1985) 211–214.
- [9] H.Y. Li, H.W. Yu, L. Sun, J.L. Zhai, X.R. Han, Nanoscale 7 (2015) 1610–1615.
- [10] Z.Y. Jin, Q.T. Zhang, L. Hu, J.Q. Chen, X. Cheng, Y.J. Zeng, S.C. Ruan, T. Ohno, Appl. Catal. B: Environ. 205 (2017) 569–575.
- [11] P.Y. Kuang, P.X. Zheng, Z.Q. Liu, J.L. Lei, H. Wu, N. Li, T.Y. Ma, Small 12 (2016) 6735–6744.
- [12] T. Baran, S. Wojtyla, A. Dibenedetto, M. Aresta, W. Macyk, Appl. Catal. B: Environ. 178 (2015) 170–176.
- [13] K. Maeda, K. Domen, Chem. Mater. 22 (2010) 612–623.
- [14] X.X. Hu, C. Hu, T.W. Peng, X.F. Zhou, J.H. Qu, Environ. Sci. Technol. 44 (2010) 7058–7062.

[15] X.C. Wang, K. Maeda, A. Thomas, K. Takanabe, G. Xin, J.M. Carlsson, K. Domen, M. Antonietti, *Nat. Mater.* 8 (2009) 76–80.

[16] G.G. Zhang, Z.A. Lan, L.H. Lin, S. Lin, X.C. Wang, *Chem. Sci.* 7 (2016) 3062–3066.

[17] K. Wang, Q. Li, B.S. Liu, B. Cheng, W.K. Ho, J.G. Yu, *Appl. Catal. B: Environ.* 176 (2015) 44–52.

[18] M. Zhang, W.J. Jiang, D. Liu, J. Wang, Y.F. Liu, Y.Y. Zhu, Y.F. Zhu, *Appl. Catal. B: Environ.* 183 (2016) 263–268.

[19] W.J. Wang, J.C. Yu, D.H. Xia, P.K. Wong, Y.C. Li, *Environ. Sci. Technol.* 47 (2013) 8724–8732.

[20] S.F. Chen, Y.F. Hu, S.G. Meng, X.L. Fu, *Appl. Catal. B: Environ.* 150 (2014) 564–573.

[21] M. Zhang, J. Xu, R.L. Zong, Y.F. Zhu, *Appl. Catal. B: Environ.* 147 (2014) 229–235.

[22] M.W. Zhang, X.C. Wang, *Energy Environ. Sci.* 7 (2014) 1902–1906.

[23] Y.-S. Jun, J. Park, S.U. Lee, A. Thomas, W.H. Hong, G.D. Stucky, *Angew. Chem. Int. Ed.* 52 (2013) 11083–11087.

[24] K. Pandiselvi, H.F. Fang, X.B. Huang, J.Y. Wang, X.C. Xu, T. Li, *J. Hazard. Mater.* 314 (2016) 67–77.

[25] S.K. Le, T.S. Jiang, Q. Zhao, X.F. Liu, Y.Y. Li, B.W. Fang, M. Gong, *RSC Adv.* 6 (2016) 38811–38819.

[26] S.K. Le, T.S. Jiang, Y.W. Li, Q. Zhao, Y.Y. Li, B.W. Fang, M. Gong, *Appl. Catal. B: Environ.* 200 (2017) 601–610.

[27] R. Prins, M.E. Bussell, *Catal. Lett.* 142 (2012) 1413–1436.

[28] H. Song, J. Wang, Z. Wang, H. Song, F. Li, Z. Jin, *J. Catal.* 311 (2014) 257–265.

[29] A.M. Alexander, J.S.J. Hargreaves, *Chem. Soc. Rev.* 39 (2010) 4388–4401.

[30] C.G. Morales-Guio, L.-A. Stern, X. Hu, *Chem. Soc. Rev.* 43 (2014) 6555–6569.

[31] E.J. Popczun, J.R. McKone, C.G. Read, A.J. Biacchi, A.M. Wiltrot, N.S. Lewis, R.E. Schaak, *J. Am. Chem. Soc.* 135 (2013) 9267–9270.

[32] H.P. Andaraarachchi, M.J. Thompson, M.A. White, H.J. Fan, J. Vela, *Chem. Mater.* 27 (2015) 8021–8031.

[33] Z.J. Sun, H.F. Zheng, J.S. Li, P.W. Du, *Energy Environ. Sci.* 8 (2015) 2668–2676.

[34] S. Cao, Y. Chen, C.J. Wang, P. He, W.F. Fu, *Chem. Commun.* 50 (2014) 10427–10429.

[35] Y.B. Chen, Z.X. Qin, *Catal. Sci. Technol.* 6 (2016) 8212–8822.

[36] A. Indra, A. Acharjya, P.W. Menezes, C. Merschjann, D. Hollmann, M. Schwarze, M. Aktas, A. Friedrich, S. Lochbrunner, A. Thomas, M. Driess, *Angew. Chem. Int. Ed.* 56 (2017) 1653–1657.

[37] X. Wang, S. Blechert, M. Antonietti, *ACS Catal.* 2 (2012) 1596–1606.

[38] Y.Y. Deng, Y. Zhou, Y. Yao, J. Wang, *New J. Chem.* 37 (2013) 4083–4088.

[39] D.M. Chen, K.W. Wang, W.Z. Hong, R.L. Zong, W.Q. Yao, Y.F. Zhu, *Appl. Catal. B: Environ.* 166–167 (2015) 366–373.

[40] W.J. Wang, Y. Yu, T.C. An, G.Y. Li, H.Y. Yip, J.C. Yu, P.K. Wong, *Environ. Sci. Technol.* 46 (2012) 4599–4606.

[41] Z.A. Lan, G.G. Zhang, X.C. Wang, *Appl. Catal. B: Environ.* 192 (2016) 116–125.

[42] J.J. Xue, S.S. Ma, Y.M. Zhou, Z.W. Zhang, M. He, *ACS Appl. Mater. Interfaces* 7 (2015) 9630–9637.

[43] S.J. Liang, Y.Z. Xia, S.Y. Zhu, S. Zheng, Y.H. He, J.H. Bi, M.H. Liu, L. Wu, *Appl. Surf. Sci.* 358 (2015) 304–312.

[44] A. Panneerselvam, M.A. Malik, M. Afzaal, P. O'Brien, M. Helliwell, *J. Am. Chem. Soc.* 130 (2008) 2420–2421.

[45] J. Liu, Y. Liu, N. Liu, Y. Han, X. Zhang, H. Huang, Y. Lifshitz, S.T. Lee, J. Zhong, Z. Kang, *Science* 347 (2015) 970–974.

[46] R. Kuriki, K. Sekizawa, O. Ishitani, K. Maeda, *Angew. Chem. Int. Ed.* 54 (2015) 2406–2409.

[47] H. Liu, Z.Z. Xu, Z. Zhang, D. Ao, *Appl. Catal. B: Environ.* 192 (2016) 234–241.

[48] H. Song, M. Dai, H.L. Song, X. Wan, X.W. Xu, Z.S. Jin, *J. Mol. Catal. A: Chem.* 385 (2014) 149–159.

[49] K. Senevirathne, A.W. Burns, M.E. Bussell, S.L. Brock, *Adv. Funct. Mater.* 17 (2007) 3933–3939.

[50] S. Carencio, C. Boissière, L. Nicole, C. Sanchez, P.L. Floc'h, N. Mézailles, *Chem. Mater.* 22 (2010) 1340–1349.

[51] Y.P. Zhu, T.Z. Ren, Z.Y. Yuan, *ACS Appl. Mater. Interfaces* 7 (2015) 16850–16856.

[52] Y. Zhang, T. Mori, J. Ye, M. Antonietti, *J. Am. Chem. Soc.* 132 (2010) 6294–6295.

[53] J. Zhang, M. Zhang, G. Zhang, X. Wang, *ACS Catal.* 2 (2012) 940–948.

[54] Q.Y. Lin, L. Li, S.J. Liang, M.H. Liu, J.H. Bi, L. Wu, *Appl. Catal. B: Environ.* 163 (2015) 135–142.

[55] Y.R. Liu, W.H. Hu, X. Li, B. Dong, X. Shang, G.Q. Han, Y.M. Chai, Y.Q. Liu, C.G. Liu, *Appl. Surf. Sci.* 383 (2016) 276–282.

[56] Z.P. Huang, Z.B. Chen, Z.Z. Chen, C.C. Lv, H. Meng, C. Zhang, *ACS Nano* 8 (2014) 8121–8129.

[57] Z. Pu, Q. Liu, C. Tang, A.M. Asiri, X. Sun, *Nanoscale* 6 (2014) 11031–11034.

[58] S. Cao, Y. Chen, C.J. Wang, P. He, W.F. Fu, *Chem. Commun.* 50 (2014) 10427–10429.

[59] S.W. Cao, J. Jiang, B.C. Zhu, J.G. Yu, *Phys. Chem. Chem. Phys.* 18 (2016) 19457–19463.

[60] Z. Han, F. Qiu, R. Eisenberg, P.L. Holland, T.D. Krauss, *Science* 338 (2012) 1321–1324.

[61] A.H. Geeraerd, C.H. Herremans, J.F. Van Impe, *Int. J. Food Microbiol.* 59 (2000) 185–209.

[62] W.J. Wang, L.Z. Zhang, T.C. An, G.Y. Li, H.Y. Yip, P.K. Wong, *Appl. Catal. B: Environ.* 108–109 (2011) 108–116.

[63] W.J. Wang, T.W. Ng, W.K. Ho, J.H. Huang, S.J. Liang, T.C. An, G.Y. Li, J.C. Yu, P.K. Wong, *Appl. Catal. B: Environ.* 129 (2013) 482–490.

[64] J. Li, Y.C. Yin, E.Z. Liu, Y.G. Ma, J. Wan, J. Fan, X.Y. Hu, *J. Hazard. Mater.* 321 (2017) 183–192.

[65] P. Madhusudan, J.R. Ran, J. Zhang, J.G. Yu, G. Liu, *Appl. Catal. B: Environ.* 110 (2011) 286–295.

[66] E.J. Popczun, J.R. McKone, C.G. Read, A.J. Biacchi, A.M. Wiltrot, N.S. Lewis, R.E. Schaak, *J. Am. Chem. Soc.* 135 (2013) 9267–9270.

[67] G.Y. Li, X. Nie, Y.P. Gao, T.C. An, *Appl. Catal. B: Environ.* 180 (2016) 726–732.

[68] G.Y. Li, X. Nie, J.Y. Chen, Q. Jiang, T.C. An, P.K. Wong, H.M. Zhang, H.J. Zhao, H. Yamashita, *Water Res.* 86 (2015) 17–24.

[69] W.Q. Li, X. Liu, H.X. Li, *J. Mater. Chem. A* 3 (2015) 15214–15224.